# Thermal conductivity of crystalline Ge2Sb2Te5: lattice contribution and size effects in the cubic phase quantified by approach-to-equilibrium molecular dynamics

Ibrahim Bel-Hadj, Mohammed Guerboub, Achille Lambrecht, Guido Ori, Carlo Massobrio, Évelyne Martin

Journal of Physics D: Applied Physics

**ACCEPTED MANUSCRIPT**

# Thermal conductivity of crystalline $Ge_2Sb_2Te_5$: lattice contribution and size effects in the cubic phase quantified by approach-to-equilibrium molecular dynamics

To cite this article before publication: Ibrahim Bel-Hadj *et al* 2024 *J. Phys. D: Appl. Phys.* in press https://doi.org/10.1088/1361-6463/ad316b

# Thermal conductivity of crystalline $Ge_2Sb_2Te_5$: lattice contribution and size effects in the cubic phase quantified by approach-to-equilibrium molecular dynamics

**Ibrahim Bel-Hadj**
Université de Strasbourg, CNRS, Laboratoire ICube, UMR 7357, F-67037 Strasbourg, France

**Mohammed Guerboub**
Université de Strasbourg, CNRS, Institut de Physique et Chimie des Matériaux de Strasbourg, UMR 7504, Strasbourg F-67034, France

**Achille Lambrecht**
Université de Strasbourg, CNRS, Laboratoire ICube, UMR 7357, F-67037 Strasbourg, France
Université de Strasbourg, CNRS, Institut de Physique et Chimie des Matériaux de Strasbourg, UMR 7504, Strasbourg F-67034, France

**Guido Ori**
Université de Strasbourg, CNRS, Institut de Physique et Chimie des Matériaux de Strasbourg, UMR 7504, Strasbourg F-67034, France

**Carlo Massobrio**
Université de Strasbourg, CNRS, Laboratoire ICube, UMR 7357, F-67037 Strasbourg, France

**Evelyne Martin**
E-mail: evelyne.martin@unistra.fr
Université de Strasbourg, CNRS, Laboratoire ICube, UMR 7357, F-67037 Strasbourg, France

ADynMat consortium
https://www.adynmat.cnrs.fr

December 2023

**Abstract.** Approach-to-equilibrium molecular dynamics simulations are carried out for the cubic phase of crystalline $Ge_2Sb_2Te_5$, using interatomic forces derived from a machine learning interatomic potential (MLIP) trained with ab initio calculations. The use of this MLIP potential significantly reduces the computational burden, allowing for the study of systems over 70 nanometers in length. Above 20 nm, the thermal conductivity of the lattice plateaus at 0.37

± 0.01 W $K^{-1}$ $m^{-1}$ in agreement with measurements reported in the literature. However, below 20 nm, size effects lead to a reduction in thermal conductivity which is systematically calculated.

*Keywords*: molecular dynamics, thermal conductivity, crystalline $Ge_2Sb_2Te_5$, size effects

Submitted to: *J. Phys. D: Appl. Phys.*

## 1. Introduction

$Ge_2Sb_2Te_5$ (GST) is a non-stoichiometric chalcogenide that belongs to the phase-change material family [1]. It demonstrates rapid switching times (in between 10 and 100 ns) [2, 3] between the metastable crystalline phase, which displays cubic symmetry, and the amorphous phase. These phases exhibit marked differences in optical index, electrical resistivity, and thermal conductivity. In devices like phase-change memories, which use differences in electrical resistivity to encode binary information, the transition occurs by Joule heating with an electric current intensity and a pulse duration adapted to switch from the crystalline phase to the amorphous phase or vice versa. In particular, the transition from crystal to amorphous goes through a melting stage (Fig. 1.a). To reach the melting temperature, the electrical current has to be carefully chosen by avoiding suboptimal power consumption and destruction due to overheating. Indeed, controlling heat flow is crucial in device design and requires knowledge of the thermal conductivity. Also, devices can be miniaturized to reduce power consumption and increase their density. When designing smaller devices, the question arises whether, in addition to reducing the size of the active layer (as shown in Fig. 1.b), a decrease of the thermal conductivity at the nanoscale comes also into play (Fig. 1.c).

In this work, we examine how size impacts the thermal conductivity of the crystalline phase by employing atomic scale molecular dynamics simulations to complement experimental techniques that cannot give access to thermal properties below 30 nm. To this end, we take advantage of the approach to equilibrium molecular dynamics (AEMD) methodology [4]. The AEMD is based on the simulation of a thermal transient in conditions modelled by the heat equation in one direction and considering a periodicity. The transient decay time is related to the thermal conductivity $\kappa$. The dependence of $\kappa$ on the period $L$, which is ascribed to the supercell dimension in the heat transport direction, is documented in several of our works. The thermal conductivity increases systematically with $L$ [4, 5] and its saturation above a threshold has been observed in nanostructures [6]. This behaviour is understood as a signature of ballistic effects occurring at small dimensions with a threshold value depending on the material.

We target in the present work the lattice thermal conductivity of the cubic phase of crystalline GST (cGST). The interactions are modelled by a machine-learned interatomic potential (MLIP) trained on an ab initio potential energy surface [7]. This choice is motivated by the expectation that size effects in the crystalline phase of GST will persist at largest sizes than in amorphous GST (aGST). These effects have recently been addressed for aGST by first-principles molecular dynamics (FPMD) [5]. We have shown that for the largest cells affordable by FPMD, i. e. for a $\sim$1000 atoms model with a length in the heat direction of $L \approx 8$ nm, the thermal conductivity is not yet saturated.

In the following, the computational method is presented in Section 2. Results on the thermal conductivity are presented and discussed in Section 3. Conclusions are drawn in Section 4.

## 2. Computational method

We employed the MLIP based on the Gaussian Approximation Potential (GAP) scheme [8] developed by Mocanu et al. [7]. The MLIP is made of two descriptors for the atomic structure: a nonparametric two-body term and the smooth overlap of atomic positions (SOAP) [9]. The fit is performed on a data base sampling local environments collected from FPMD trajectories in the liquid, amorphous and partially crystallized states. Several crystalline elemental phases (Ge, Sb or Te), binary constituents (GeTe and $Sb_2Te_3$) and a crystalline GST phase are also included for the training. All DFT data were obtained with the projector augmented-wave method and are detailed in Ref. [7]. Mocanu et al. also demonstrated the capability of their MLIP to predict the crystallization into the cubic crystalline phase of interest in the present study. Therefore it appears appropriate to employ this methodology for the calculation of thermal conductivity via molecular dynamics.

Our MD simulations are performed by using the LAMMPS code [10] compiled with QUIP module [11] including GAP [12]. The time step is set to 1 fs. The atomic model is the cubic phase of cGST featuring $Fm\bar{3}m$ symmetry [13]. Te atoms occupy one site, whereas the other site is randomly occupied by Ge, Sb, and vacancies, resulting in a Ge+Sb:Te ratio of 4:5. An example of local structure around a vacancy, captured at finite temperature during the

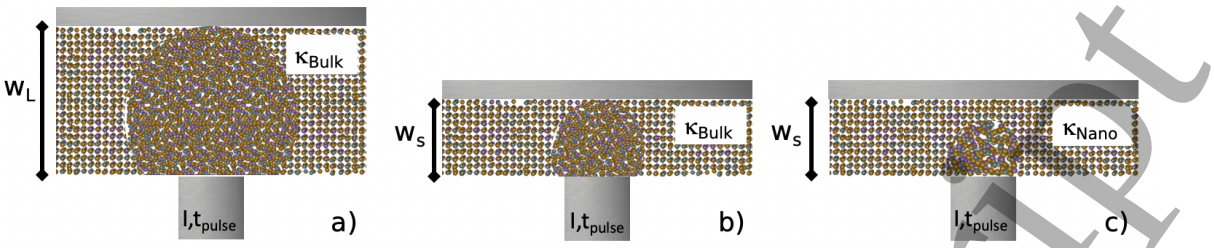


**Figure 1.** Schematic of the local melting in a phase-change device after application of an electric current $I$ during a time $t_{\mathrm{pulse}}$. $I$ and $t_{\mathrm{pulse}}$ have been selected such that melting can occur in the large width ($w_{\mathrm{L}}$) case. a) Large width ($w_{\mathrm{L}}$) and bulk thermal conductivity ($\kappa_{\mathrm{Bulk}}$). b) Small width $w_{\mathrm{s}} < w_{\mathrm{L}}$ and $\kappa_{\mathrm{Bulk}}$. c) $w_{\mathrm{s}} < w_{\mathrm{L}}$ and nanoscale thermal conductivity $\kappa_{\mathrm{Nano}} < \kappa_{\mathrm{Bulk}}$.

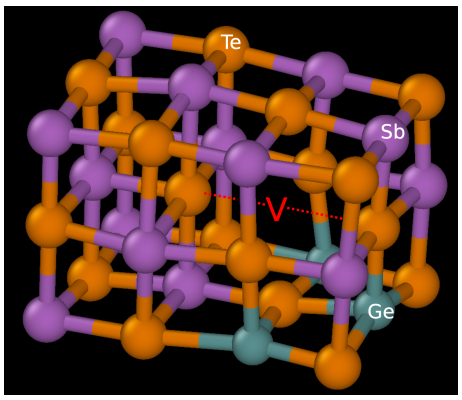


**Figure 2.** View of the lattice structure arrangement, with Te, Ge and Sb atoms at the nodes of two interpenetrating (for Te and Ge/Sb respectively) cubic lattices. Due to the chosen stoichiometry, vacancies do exist intrinsically as highlighted by a red "V".

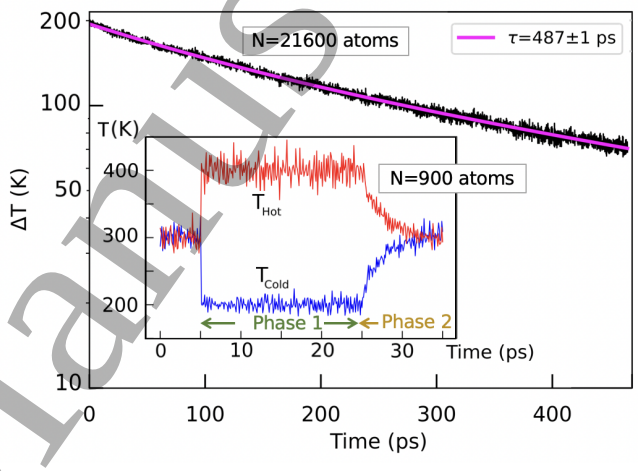


**Figure 3.** Temperature difference $\Delta T = T_{\mathrm{Hot}} - T_{\mathrm{Cold}}$ between the hot and cold blocks during phase 2 (in black), plotted on a logarithmic scale to highlight its exponential nature (fit shown in magenta, with a decay time $\tau = 487 \pm 1$ ps). Case of the largest supercell of length $L_z$= 73 nm containing 21600 atoms. In the inset, $T_{\mathrm{Hot}}$ (red line) and $T_{\mathrm{Cold}}$ (blue line) during the equilibrium run at room temperature, followed by phase 1 and phase 2 of the AEMD. Case of the small supercell of length $L_z$= 3 nm containing 900 atoms.

thermal transient, is shown in Fig. 2. The density is initially set to the experimental value (6.3 g cm$^{-3}$) [13]. After a trajectory lasting 10 ps in the isobaric-isothermal ensemble at zero pressure ($P = 0$ GPa) and room temperature ($T = 300$ K), and using periodic boundary conditions in the three directions, the lattice parameter increases by 1% and the density decreases to 6.1 g cm$^{-3}$. This slight (3%) difference from the experimental value reflects the accuracy of the selected MLIP [7]. Atomic orthorhombic supercells are built using a multiple of the lattice constant at zero pressure. The dimensions along the $x$ and $y$ directions are set to 3 nm. The length in the $z$ direction bound to be the direction of heat transport ranges from $L_z$=3 to 73 nm. This corresponds to supercells made of 900 up to 21600 atoms.

After a short trajectory (5 ps) at room temperature, the AEMD methodology is applied. In phase 1, a non-equilibrium configuration is created, by imposing a local thermostat to each of two parts of the box delimited along the $z$ direction. The target temperature of the thermostats are set to $T = 200$ K and $T = 400$ K respectively. The average temperatures of the hot and cold blocks are shown in the inset of Fig. 3. The target temperatures are reached rapidly. The thermostats are kept for at least 10 ps, resulting in an almost step-like temperature profile (Fig. 4), and then released to allow beginning the phase 2. Phase 2 is characterised by a transient in which the hot part cools down while the cold part heats up, ending up with a uniform temperature throughout the system.

The heat transport regime simulated above corresponds to the transient of the heat equation in one direction:

$$\frac{\partial T(t,z)}{\partial t} = \frac{\kappa}{c_v}\frac{\partial^2 T(t,z)}{\partial z^2} \qquad (1)$$

with $\kappa$ the thermal conductivity and $c_v$ the volumetric heat capacity. For systems with periodic boundary conditions, such as in our MD simulations, the

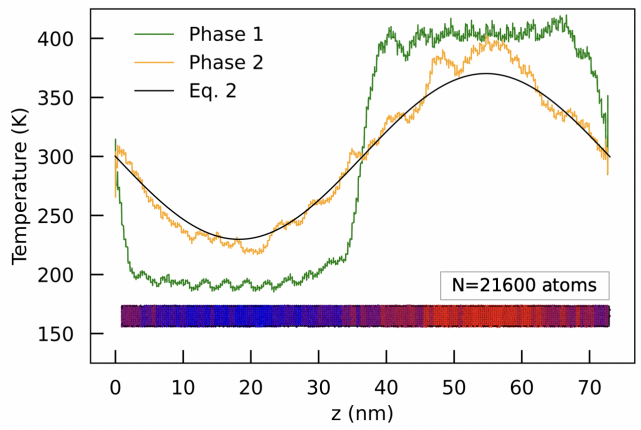


**Figure 4.** Temperature profile along the heat transport direction $z$ at the end of phase 1 (in green) and at 265 ps after the beginning of phase 2 (in orange). The supercell of length $L_z$= 73 nm contains $N = 21600$ atoms displayed at the bottom. The color code (that goes from blue for $T = 200$ K to red for $T = 400$ K) corresponds to the local temperature, calculated for steps of 7 nm in the $z$ direction.

analytical solution of Eq. 1 is the Fourier series [4]:

$$T(t,z) = T_{\text{av}} + \sum_{n=0}^{\infty} \frac{2\Delta T_0}{(2n+1)\pi} \sin\left(2\pi(2n+1)\frac{z}{L_z}\right) e^{-(2n+1)^2 t/\tau} \quad (2)$$

where $T_{\text{av}} = 300$ K is the average temperature, and $\Delta T_0 = 200$ K is the initial difference of temperature between the hot block and the cold one. The decay time $\tau$ is equal to:

$$\tau = \frac{L_z^2}{4\pi^2}\frac{c_v}{\kappa} \quad (3)$$

The predominant contribution of the series (Eq. 2) for $n = 0$ is equal to:

$$T(t,z) = T_{\text{av}} + \frac{2\Delta T_0}{\pi} \sin\left(2\pi\frac{z}{L_z}\right) e^{-t/\tau}. \quad (4)$$

The temperature profile, approximated using the dominant contribution of the Fourier series, is displayed in Fig. 4 concurrently with the molecular dynamics calculation. The level of agreement between the two is highly satisfactory, indicating that we can confine ourselves to the dominant term in order to interpret results obtained from molecular dynamics. This involves omitting the terms for $n \geq 1$ in Eq. 3. We obtain a temperature difference between the average temperature of the hot block $T_{\text{Hot}}(t)$ :

$$T_{\text{Hot}}(t) = \frac{1}{L_z/2}\int_{z=L_z/2}^{L_z} T(t,z)dz \quad (5)$$

and the average temperature of the cold block $T_{\text{Cold}}(t)$ :

$$T_{\text{Cold}}(t) = \frac{1}{L_z/2}\int_{z=0}^{L_z/2} T(t,z)dz \quad (6)$$

given by $\Delta T(t) = T_{\text{Hot}}(t) - T_{\text{Cold}}(t) = \Delta T_0 e^{-t/\tau}$. Fig. 3 features, as an illustration, the exponential fit (magenta line) used to extract the transient decay time $\tau$ in the system containing $N = 21600$ atoms. From time $\tau$, the thermal conductivity $\kappa$ can be obtained by inverting Eq. 3:

$$\kappa = \frac{L_z^2}{4\pi^2}\frac{c_v}{\tau}. \quad (7)$$

To calculate $c_v = \frac{1}{V}\left(\frac{\partial U}{\partial T}\right)_V$, we collected the total energy $U$ at temperatures of $T = 100$, 300 and 500 K and constant volume $V$, over a few ps. The result obtained is close to the Dulong and Petit value ($3Nk_B/V$) with a small correction factor of $\gamma = 1.048$.

The two-phase procedure is repeated for each of the eight boxes of length $L_z$ ranging from 3 to 73 nm. Phase 1 always lasts approximately 10 ps, which is adequate to generate the hot and cold blocks, regardless of the system size. The duration of phase 2 depends on the size of the system via $L_z$, $c_v$ and $\kappa$ should this variable not to be constant (Eq. 3). Phase 2 is extended until the exponential fit is stationary, this meaning that $\tau$ corresponding to the time interval in between $t = 0$ to $t = t_n$ does not change significantly when the time interval considered is in between $t = 0$ to $t = t_{n+1}$, where $t_{n+1} \gg t_n$). This occurs typically for a temperature difference $\Delta T$ of 70 K or less. To assess the statistical error, and in particular for the smaller systems affected by larger temperature fluctuations, several other phases 1 and 2 allow providing additional determinations of $\tau$ and, therefore, of the thermal conductivity $\kappa$.

## 3. Results and discussion

The thermal conductivity, ascertained via Eq. 7, is presented in Fig. 5 as a function of the length of the supercell in the heat transport direction. The values rise alongside $L_z$, achieving a saturation point of 0.37±0.01 W m$^{-1}$ K$^{-1}$ for $L_z \geq 20$ nm.

Thermal conductivity measurements of cGST films have been documented in the existing literature, for both in-plane [15] and cross-plane [16, 14] heat transport. Lee et al. [14] measured the cross-plane thermal conductivity on films with thicknesses of 30 and 150 nm. The results were identical for both thicknesses, in agreement with our calculations indicating that there is no variation of the thermal conductivity beyond 20 nm. The overall thermal conductivity, encompassing the lattice and electronic contributions, is equal to 0.45±0.09 W m$^{-1}$ K$^{-1}$, which is consistent with the value of 0.45 W m$^{-1}$ K$^{-1}$ reported by Yang et al. [15] for in-plane thermal transport. This agreement shows that the thermal conductivity of the bulk is obtained in both scenarios, by ruling out important surface effects. Lee et al.

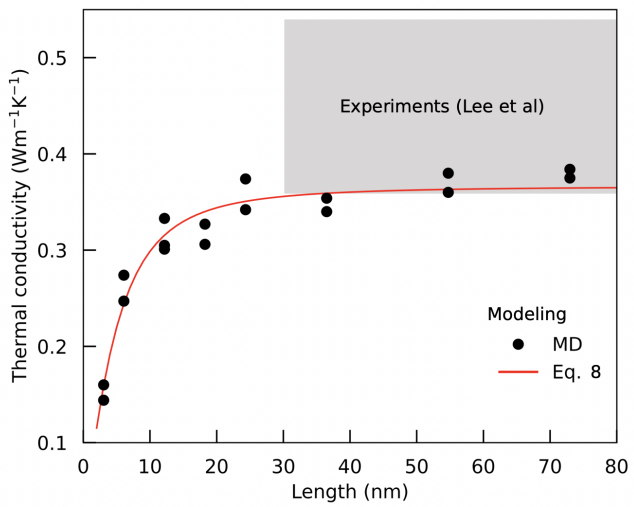


**Figure 5.** Thermal conductivity of cGST versus the length of the supercell in the heat transport direction. The points are the results of our MD simulations (lattice thermal conductivity). The red line is a physical model of size effects fitted to our results. The grey area represents the measurements of Lee et al. [14] for the total thermal conductivity.

[14] have estimated the electronic contribution to the thermal conductivity to 0.04 W m$^{-1}$ K$^{-1}$, by using the Wiedemann-Franz law with the measured electrical resistivity. This amounts to a lattice contribution of 0.41±0.09 W m$^{-1}$ K$^{-1}$. Our result for $L_z \geq 20$ nm (0.37±0.01 W m$^{-1}$ K$^{-1}$), obtained without considering the electronic contribution, is in excellent agreement with this value.

Our results have provided evidence that size effects become apparent below 20 nm. It is worth noting that this is already observable in silicon crystals at 10 $\mu$m (for instance, see Ref. [17]), this threshold being relatively low. The underlying phenomenon occurs when the size of a system is smaller than the maximum value of the distribution of phonon mean free paths (MaxMFP). In such cases, phonons that would otherwise be scattered in bulk systems experience ballistic trajectories. One can assume that chemical disorder at one of the sites in the cubic lattice (Ge, Sb or vacancy) is at the origin of the low value of the MaxMFP in cGST.

Alvarez and Jou [18] put forth a formula that accounts for size effects by incorporating a combination of ballistic and diffusive phonon propagation. This formula is nicely consistent with our molecular dynamics calculations, as demonstrated in Fig. 5. Consequently, changes in thermal conductivity with respect to size can be easily quantified by:

$$\kappa(L) = \kappa_{\text{Bulk}} \frac{L^2}{2\pi^2 l^2} \left[ \sqrt{1 + 4\left(\frac{\pi l}{L}\right)^2} - 1 \right] \qquad (8)$$

with $\kappa_{\text{Bulk}} = 0.37$ W m$^{-1}$ K$^{-1}$ and $l = 1.7 \pm 0.1$ nm fitted on our AEMD results.

From the standpoint of applications, our results indicate that case c) in Fig. 1 will indeed apply when the layer thickness decreases below 20 nm, fully within the reach of present technological fabrication processes. During the electrical pulse of amplitude $I$ and duration $t_{\text{pulse}}$, designed to induce the crystal-liquid transition by Joule heating, a reduction in the thermal conductivity results in an incomplete melting of the layer over its entire thickness. After cooling, the electrical conduction path will consist of both an amorphous portion, which has lower electrical conductivity, and a crystalline portion, which has higher electrical conductivity. Therefore, the difference of electric resistance between the two states used to encode binary information will be less noticeable. Eq. 8, fitted to our calculations, will allow to adapt the design of the device, and in particular, to determine the new optimal values of $I$ and $t_{\text{pulse}}$.

From a methodology standpoint, the current study illustrates that using a MLIP to calculate thermal conductivity produces results that are just as quantitative as those achieved in our earlier investigations with FPMD, particularly for the amorphous phase of $Ge_2Sb_2Te_5$. Moreover, employing this method has enhanced calculation speed and enabled us to attain saturation in the $\kappa(L)$ graphs produced via the AEMD technique, which is a seldom-seen event. Indeed, AEMD was first used for crystals, including silicon described applying Tersoff's empirical potential [19]. In that case, the saturation of the $\kappa(L)$ graph was not observed even at $L \approx 2\mu m$, due to size effects that limit saturation. We extrapolated the bulk thermal conductivity using the Alvarez and Jou law, but the resulting value [20] of 110±3 W m$^{-1}$ K$^{-1}$ at a temperature of 500 K was found to overestimate measurements [21] of 80 W m$^{-1}$ K$^{-1}$. This discrepency can be ascribed to the quantitative restrictions inherent in empirical potentials when modelling materials. To achieve higher predictive power, FPMD was also utilised to simulate thermal transients in AEMD. Nevertheless, the account of the electronic structure in FPMD led to limitations on computational workload, which ultimately curtailed the size of affordability to about 8 nm. For amorphous $Ge_2Sb_2Te_5$, thermal conductivities can extend to 0.2 W K$^{-1}$ m$^{-1}$ while computed within the 2-8 nm scale [5]. This accounts for roughly 75% of the bulk value. The use of machine-learned interatomic potentials is a promising route for handling the description and impact of size effects in thermal transport while maintaining predictability.

## 4. Conclusion

We have employed the approach-to-equilibrium molecular dynamics methodology to calculate and monitor with size the lattice thermal conductivity of the cubic phase of $Ge_2Sb_2Te_5$ phase-change materials. The thermal conductivity aligns with the experimental finding for sizes greater than 20 nm. A decrease in thermal conductivity is apparent for sizes less than 20 nm. Our calculations have been used to parameterize a physical law, allowing for the effective simulation of thermal management in devices that exploits phase-change materials.

## Acknowledgments

This work was funded by the French National Research Agency (ANR) through the Programme d'Investissement d'Avenir under contract ANR-11-LABX-0058_NIE and ANR-17-EURE-0024 within the Investissement d'Avenir program ANR-10-IDEX-0002-02. M.G. also received support from the QUSTEC program (European Union Horizon 2020, Marie Skłodowska-Curie Grant Agreement No. 847471).The authors would like to acknowledge the High Performance Computing Center of the University of Strasbourg for supporting this work by providing scientific support and access to computing resources. Part of the computing resources were funded by the Equipex Equip@Meso project (Programme Investissements d'Avenir) and the CPER Alsacalcul/Big Data. Calculations on the larger systems were performed by using resources from GENCI (Grand Equipement National de Calcul Intensif) (Grant A0**0910296 and A0**0905071).

## Data availability

The data that support the findings of this study are available from the corresponding author upon reasonable request.

## References

[1] Joshi V, Le Gallo M, Haefeli S, Boybat I, Nandakumar S R, Piveteau C, Dazzi M, Rajendran B, Sebastian A and Eleftheriou E 2020 *Nature Communications* **11** 2473

[2] Perego S, Dragoni D, Gabardi S, Campi D and Bernasconi M 2023 *physica status solidi (RRL) - Rapid Research Letters* **17** 2200433

[3] Kheir O A E, Bonati L, Parrinello M and Bernasconi M 2023 Unraveling the crystallization kinetics of the $Ge_2Sb_2Te_5$ phase change compound with a machine-learned interatomic potential (*Preprint* 2304.03109)

[4] Lampin E, Palla P L, Francioso P A and Cleri F 2013 *Journal of Applied Physics* **114** 033525

[5] Duong T Q, Bouzid A, Massobrio C, Ori G, Boero M and Martin E 2021 *RSC Advances* **11** 10747–10752

[6] Zaoui H, Palla P L, Giordano S, Cleri F, Verdier M, Lacroix D, Robillard J F, Termentzidis K and Martin E 2018 *International Journal of Heat and Mass Transfer* **126** 830–835

[7] Mocanu F C, Konstantinou K, Lee T H, Bernstein N, Deringer V L, Csányi G and Elliott S R 2018 *The Journal of Physical Chemistry B* **122** 8998–9006

[8] Bartók A P, Payne M C, Kondor R and Csányi G 2010 *Phys. Rev. Lett.* **104**(13) 136403

[9] Bartók A P, Kondor R and Csányi G 2013 *Phys. Rev. B* **87**(18) 184115

[10] Thompson A P, Aktulga H M, Berger R, Bolintineanu D S, Brown W M, Crozier P S, in 't Veld P J, Kohlmeyer A, Moore S G, Nguyen T D, Shan R, Stevens M J, Tranchida J, Trott C and Plimpton S J 2022 *Comp. Phys. Comm.* **271** 108171

[11] https://libatoms.github.io

[12] Mocanu F and Konstantinou K 2018 URL `https://www.repository.cam.ac.uk/handle/1810/279038`

[13] Matsunaga T, Yamada N and Kubota Y 2004 *Acta Crystallographica Section B* **60** 685–691

[14] Lee J, Bozorg-Grayeli E, Kim S, Asheghi M, Philip Wong H S and Goodson K E 2013 *Applied Physics Letters* **102** 191911

[15] Yizhang Yang H F H and Asheghi M 2009 *Nanoscale and Microscale Thermophysical Engineering* **13** 88–98

[16] Battaglia J L, Kusiak A, Schick V, Cappella A, Wiemer C, Longo M and Varesi E 2010 *Journal of Applied Physics* **107** 044314

[17] Regner K T, Sellan D P, Su Z, Amon C H, McGaughey A J and Malen J A 2013 *Nature Communications* **4** 1640

[18] Alvarez F X and Jou D 2007 *Applied Physics Letters* **90** 083109

[19] Tersoff J 1988 *Physical Review B* **38** 9902–9905

[20] Palla P L, Zampa S, Martin E and Cleri F 2019 *International Journal of Heat and Mass Transfer* **131** 932–943

[21] Glassbrenner C J and Slack G A 1964 *Phys. Rev.* **134**(4A) A1058–A1069